Constant-Envelope Modulation of Ince-Gaussian Beams for High Bandwidth Underwater Wireless Optical Communications

Evan Robertson, Danilo G. Pires, Kunjian Dai, Justin Free, Kaitlyn Kimmel, Natalia Litchinitser, J. Keith Miller, and Eric G. Johnson

***Abstract*—Wireless communication through underwater environments has become an area of increased interest in recent years. The use of Laguerre-Gaussian beams for communication through turbid environments has been well explored. We propose and demonstrate a high data rate communication method using Ince-Gaussian (IG) beams. Using the second harmonic generation process, the IG beam can be generated and modulated at gigahertz speeds. By controlling the phase matching condition of the SHG process, the coefficients of the generated modes can be controlled. Modulating the data in the phase of the beam provides constant envelope modulation. One advantage of this communication architecture is that it is power scalable. Using a 32 Quadrature Amplitude Modulated (QAM) signal, a data rate of 25 Gbit/s on a single channel was achieved with a bit error rate of 9.95×10^{-4} which is below the forward error correction limit.**

***Index Terms*—Free-space optics, optical communications, structured light, underwater communications.**

I. Introduction

THE area of underwater communications has continued to gain increasing interest in recent years. There have been a number of studies on the underwater environment, and the effect that the environment has on optical systems [1]. The effects of the environment can be characterized by three main categories: absorption, scattering, and turbulence. The effects of absorption and scattering are closely related and can be characterized by Beer's Law, $P_o = P_i \ \exp(-cz)$ where P_o is the power after the channel, P_i is the input power to the channel, c is the attenuation coefficient, and z is the propagation distance. The combined value cz is defined as attenuation length. The attenuation coefficient is the sum of the absorption, a, and the scattering, b, coefficients. This law describes the decay of an optical source as it propagates through an underwater channel. A variety of real-world environments have been studied to characterize the absorption and scattering effects of these channels [1], [2]. The impact of the underwater environment on optical channels depends on the wavelength of the transmitted light. The typical coefficients for absorption and scattering in different environments are shown in Table I [1].

TABLE I
Attenuation Coefficients

Water Types	$a(\lambda)\ m^{-1}$	$b(\lambda)\ m^{-1}$	$c(\lambda)\ m^{-1}$
Pure Sea	0.041	0.003	0.044
Clear Ocean	0.114	0.037	0.151
Coastal Ocean	0.179	0.219	0.398
Turbid Harbor	0.366	1.824	2.190

Typical absorption, $a(\lambda)$, and scattering, $b(\lambda)$, for different underwater environments. The total attenuation coefficient, $c(\lambda)$.

Blue-green light transmits best through these environments due to the low absorption and scattering of pure water [3]. The sources used to transmit data in these cases were Gaussian beams. Many different modulation schemes are shown through the different experiments, but the common result is a form of amplitude modulation. Amplitude modulation limits the power scalability of the system due to a system's high peak-to-average power ratio (PAPR). It has been shown that the signal bandwidth is not limited due to high turbidity, but it is limited by field of view [4]. Using a narrow field of view, a high bandwidth signal can be recovered through turbidity.

Along with work using Gaussian beams for data transmission, there has been work done utilizing structured light such as orbital angular momentum (OAM) as the data carrier. OAM beams are characterized by their phase profile which can be described by $\exp(il\theta)$, where l is the mode or charge number and θ is the azimuthal angular variable. A key benefit of using OAM beams is mode division multiplexing (MDM) [5]. Two channels were multiplexed where each had a data rate of up to 1.5 Gbit/s. This was expanded upon through the multiplexing of four channels, with the data rate of each channel being 10 Gbit/s [6]. These works still relied on amplitude modulation techniques. A constant envelope modulation of coherently coupled OAM

Manuscript received 3 November 2022; revised 6 February 2023; accepted 24 February 2023. Date of publication 13 March 2023; date of current version 16 August 2023. This work was supported by ONR through the MURI Program under Grant N00014-20-1-2558.

Evan Robertson, Kunjian Dai, Justin Free, Kaitlyn Kimmel, J. Keith Miller, and Eric G. Johnson are with the Micro-Photonics Laboratory at the Holcombe Department of Electrical and Computer Engineering, Clemson University, Clemson, SC 29634 USA (e-mail: edr2@g.clemson.edu; kunjiad@clemson.edu; jafree@clemson.edu; ksm@clemson.edu; jkmill@clemson.edu; ejohns8@clemson.edu).

Danilo G. Pires and Natalia Litchinitser are with the Department of Electrical and Computer Engineering, Duke University, Durham, NC 27708 USA (e-mail: danilo.gomes.pires@duke.edu; natalia.litchinitser@duke.edu).

Color versions of one or more figures in this article are available at https://doi.org/10.1109/JLT.2023.3252466.

Digital Object Identifier 10.1109/JLT.2023.3252466

introduced the potential to encode data in the phase between two beams resulting in a constant intensity profile [7]. Using orthogonal frequency division multiplexing (OFDM), a data rate of 3.072 Gbit/s was achieved. Using coherently coupled OAM (CCOAM) beams, more complex OAM combinations of amplitude and phase can be used for free space communications [8], [9]. These systems increase the spectral efficiency in encoding information. It is also possible to exploit polarization division multiplexing and OAM multiplexing to increase the bandwidth of the optical link [10]. These techniques allow multiple modes to be separated in more efficient methods.

Another form of structured light which has beneficial characteristics is an Ince Gaussian (IG) beam. IG beams provide a set of solutions to the paraxial wave equation similar to Laguerre Gaussian (LG) and Hermite Gaussian (HG) beams. IG beams maintain their intensity profiles and polarization states better than Gaussian beams when transmitted through turbid media [11]. Studies have also been done where the propagation of IG beams through atmospheric turbulence was simulated [12]. The simulated beam profile was well maintained as the turbulence strength was increased. IG beams are traditionally generated using spatial light modulators (SLM) which allow the desired intensity and phase profile to be generated. While this is a convenient way to generate IG beams, it lacks the ability to modulate the beam at high speeds and with high power. Generation of the IG beams through the SHG process allows for constant envelope modulation of the beam to be performed. The beam profile is well maintained through transmission through turbid environments allowing the constant envelope modulation to be recoverable.

In this article, a method of free space communication using IG beams through turbid environments is shown. The IG beams can be generated through a nonlinear process. This work optimizes the modes through the nonlinear process to create an IG beam. Modulating the data in the relative phase of the modes which make up the pump beam results in constant envelope modulation. The data modulation proposed offers benefits over OFDM because it is possible to avoid large peaks which could appear in the time domain signal which could introduce nonlinearities in the modulation. The phase modulation results in the rotation of the beam profile. Using passive optics, correlation can be performed to recover the signal after the underwater channel.

II. Ince-Gaussian Mode Generation

The IG beam can be analytically calculated using the general equation [13]

$$IG^{e}_{p,m}\left(\boldsymbol{r}\right)=\frac{w_0}{w\left(z\right)}\,C^{m}_{p}\left(i\xi,\epsilon\right)C^{m}_{p}\left(\eta,\epsilon\right)\exp\left(\frac{-r^2}{w^2\left(z\right)}\right)\times\exp\left(i\left(kz+\frac{k\boldsymbol{r}^2}{2R\left(z\right)}-\left(p+1\right)\operatorname{atan}\left(\frac{z}{z_R}\right)\right)\right)\tag{1}$$

where w_0 is the beam size at the beam waist, $w(z)$ is the beam size at a propagation distance z, z_R is the Rayleigh length of the beam, $k=2\pi/\lambda$ is the wave number, and r is the radial position in the field. The radius of curvature of the wavefront is $R(z)$. The degree of the IG beam is m which is the number of hyperbolic nodal lines. The order of the IG beam is p, which relates to the elliptic nodal lines through $(p-m)/2$. The radial elliptic coordinate is ξ, and the angular elliptic coordinate is η. The ellipticity parameter is ϵ. The Ince Polynomial for the even modes, C^{m}_{p}, would be replaced with S^{m}_{p} for an odd IG beam written as $IG^{o}_{p,m}$.

While IG beams can be directly generated, it is also possible to generate them through the superposition of LG beams [13]:

$$IG^{e}_{p,m}=\sum_{l,n}c_{l,n}LG^{l}_{n}\tag{2}$$

The coefficients $c_{l,n}$ are determined by the mode overlap integral between the LG and IG beams and can be calculated using

$$c_{l,n}=\iint LG^{\sigma}_{l,n}IG^{*\,\sigma'}_{p,m}dS=\delta_{\sigma',\,\sigma}\,\delta_{p,2n+l}(-1)^{n+l+\frac{p+m}{2}}\times\left[\left(1+\delta_{0,l}\right)\Gamma\left(n+l+1\right)n!\right]^{\frac{1}{2}}A^{\sigma}_{(1+\delta_{o,\sigma})/2}\left(a^{m}_{p}\right)\tag{3}$$

In these equations, l represents the topological charge and n is the radial mode of the LG beam. σ is the parity of the beam, either even or odd. $A^{\sigma}_{(1+\delta_{o,\sigma})/2}$ is the Fourier coefficient of the Ince polynomial. δ is the delta function taking on the value of 1 when the subscripts match and 0 otherwise. In Particular, the IG^{e}_{22} beam can be decomposed into three LG modes, LG^{2}_{0}, LG^{2}_{0}, and LG^{0}_{1} [14], [15]. Analytically, the LG beam can be described by

$$LG^{l}_{n}\left(\boldsymbol{r}\right)=\sqrt{\frac{2n}{\left(1+\delta_{0l}\right)\pi\left(n+|l|\right)!}}\,\frac{w_0}{w\left(z\right)}\left[\frac{\sqrt{2}r}{w\left(z\right)}\right]^{|l|}\times L^{|l|}_{n}\left(\frac{2r^2}{w^2\left(z\right)}\right)\exp\left(-\frac{r^2}{w^2\left(z\right)}\right)\times\exp\left(i\left(kz-\frac{kr^2}{2R\left(z\right)}-\left(2n+|l|+1\right)\tan^{-1}\left(\frac{z}{z_R}\right)\right)\right)\times\exp\left(il\theta\right)\tag{4}$$

where $L^{|l|}_{n}$ is the generalized Laguerre Polynomial. The LG beam can be simplified to $LG^{l}_{n}=A_{|l|,n}\,\exp(il\theta)$ where $A_{|l|,n}$ is the intensity profile of the beam and the phase profile is defined by $\exp(il\theta)$. Representing the IG beam as a superposition of the LG modes results in

$$IG^{e}_{22}=c_2\,LG^{2}_{0}+c_{-2}LG^{-2}_{0}+c_0LG^{0}_{1}\tag{5}$$

where the coefficients, $c_2=c_{-2}=0.52$ and $c_0=-0.68$, which have been shown before using four wave mixing [14].

In this work, the generation of IG beams through the superposition of LG modes are experimentally generated using the setup shown in Fig. 1

This Mach-Zehnder interferometer started with a 1064 nm source that was split using a 50/50 fiber splitter. Both paths were transmitted through fiber-coupled phase modulators before being amplified using a Nuphoton fiber amplifier. The phase modulation of the data signal will be discussed further in Section III. After amplification, both beams were transmitted

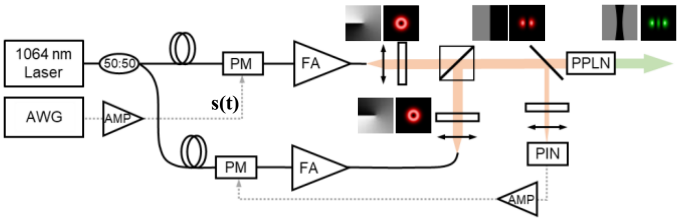

Fig. 1. The diagram of the experimental set up used to generate the IG beam through the SHG process. The pump beam is generated using a fiber, Mach-Zehnder Interferometer.

through spiral phase plates (SPP) that applied orbital angular momentum (OAM) to the beams before the second 50/50 beam splitter combined the beams. A 90/10 beam splitter is used to provide feedback to the interferometer. This feedback allows phase locking to be performed by using a low frequency phase modulator (NIR-MPX-LN-0.1) to maintain a constant relative phase between the two modes. The low frequency phase modulator has a 3dB bandwidth of 150 MHz which would correct for any random variations between the optical lengths of the two modes, but it would not respond to the modulated data. This allows only the data signal to change the relative phase between the modes. The output of the interferometer can be considered a CCOAM beam, and the field is described by

$$U_{pump}\ (r,\theta,z) = LG_n^l\ + LG_n^{-l}\exp\left(i\varphi\left(t\right)\right) \tag{6}$$

where $l = \pm 1$ is the topological charge of the OAM mode, $n = 0$ is the radial mode, and $\varphi(t)$ is the relative phase between the two modes. This CCOAM beam becomes the pump beam that generates the IG beam after pumping a periodically-poled lithium niobate (PPLN) crystal [15]

$$\begin{aligned} IG_{22}^e = U_{pump}^2 = c_2 LG_0^2\ + c_{-2} LG_0^{-2}\exp\left(i2\varphi\left(t\right)\right) \\ + c_0 LG_1^0\exp\left(i\varphi\left(t\right)\right) \end{aligned} \tag{7}$$

A relative phase difference, $2\varphi(t)$, between the two OAM modes exists. The relative phase of the LG_1^0 mode will not have any impact on the resulting beam profile. The influence of a varying relative phase can be seen in the following equation using the explicit equations of the normalized $LG_0^{|2|}$ and LG_1^0 modes for $A_{|2|,0}(r)$ and $A_{01}(r)$,

$$\begin{aligned} IG_{22}^e\ (r,\theta,t) = 2c_{|2|}\sqrt{\frac{4}{\pi}}\left(\frac{r^2}{w^3}\right)\exp\left(\frac{-r^2}{w^2}\right) \\ \times\exp\left(i\varphi\left(t\right)\right)\ \cos\left(2\theta-\varphi\left(t\right)\right) \\ + c_0\sqrt{\frac{2}{\pi}}\left(\frac{1}{w}\right)\exp\left(\frac{-r^2}{w^2}\right)\exp\left(i2\varphi\left(t\right)\right) \end{aligned} \tag{8}$$

where the explicit normalized intensity is taken from (4). The radial coordinate is *r* and the beam waist is *w*. The beam profile can be rotated by controlling the relative phase. Fig. 1(a) makes it possible to control and manipulate this relative phase difference, allowing information to be encoded on an IG beam for communication applications. Because of the propagation invariance of the IG beams, the intensity profile does not rotate or change

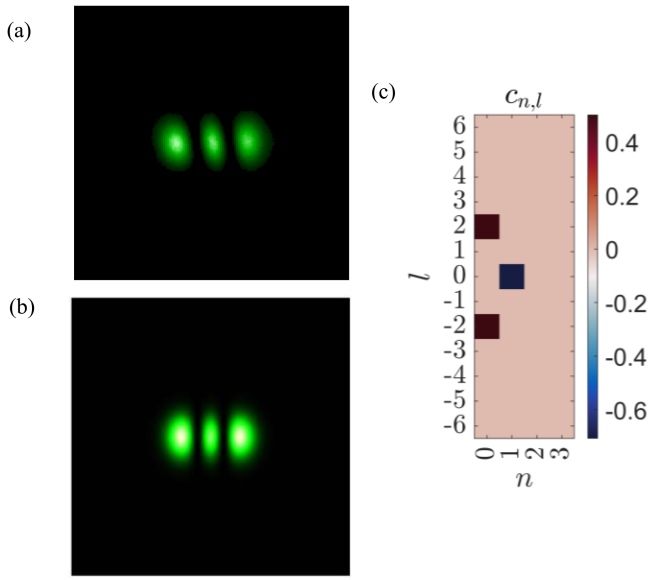

Fig. 2. (a) The experimentally generated beam through the SHG process. (b) The simulated beam through the SHG process. (c) The mode spectrum of the beams which generate the IG beam when coherently combined.

structure with propagation [12]. Therefore, the rotation of the beam profile will only be due to the applied phase modulation.

The IG beam is generated through second harmonic generation (SHG) of a collinear superposition of LG beams carrying topological charges $l = \pm 1$ and null radial order $n = 0$. The number of modes created due to nonlinear wave-mixing processes, as well as their indices, depends directly on the ratio between the length of the nonlinear crystal L and the Rayleigh length of the field z_R. Under the thin-crystal approximation ($z_R \gg L$), the coupled nonlinear evolution of the fundamental and converted frequency fields inside the crystal is negligible and the SHG field is simply the product of the input profiles related to the fundamental beam. In this case, the nonlinear crystal is large compared to the Rayleigh length ($z_R/L \approx 0.026$) and the nonlinear interactions along the propagation inside the PPLN crystal are no longer negligible. Here, the nonlinearity suppresses the creation of beams carrying different mode numbers $N_{nl} = 2n + |l| + 1$ due to the Gouy phase mismatch. One can evaluate the modes created and their weighting through the overlap integral [16], [17]

$$\Lambda_n^l = \int_{-L/2}^{L/2}\int_0^{2\pi}\int_0^R (U^\omega)^*(U^\omega)^* U_{n,l}^{2\omega}\ r dr d\theta dz \tag{9}$$

where U^ω is the fundamental field profile, and $U_{n,l}^{2\omega}$ is the upconverted field profile. Fig. 2 shows the intensity distributions of the experimental beam in Fig. 2(a), the simulated converted beam in Fig. 2(b), and the histogram containing the weighting of the generated modes in Fig. 2(c).

Controlling the phase matching condition of the SHG process, the coefficients of different modes can be controlled and tuned to the desired values. To optimize the beam as an IG beam, the coefficients have values of $c_2 = c_{-2} = 0.5$ and $c_0 = -0.7$ which are close but slightly different from those in (5). Fig. 3 shows

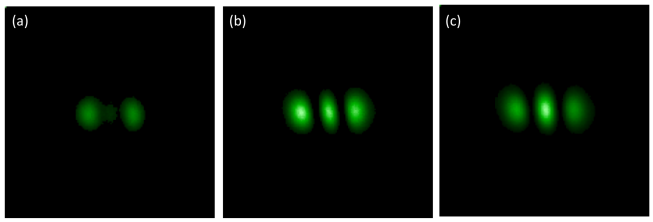

Fig. 3. Experimental beam generated through the SHG process using varying phase matching conditions of (a) $57.4\ ^{\circ}C$, (b) $60.4\ ^{\circ}C$, and (c) $61.4\ ^{\circ}C$.

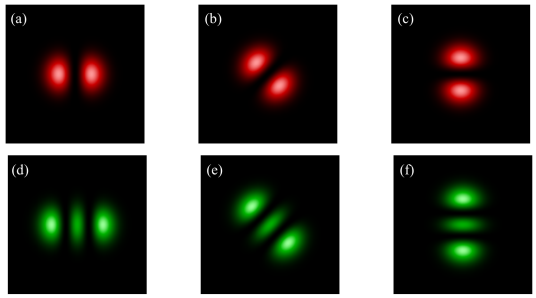

Fig. 4. Simulated beam profiles of the pump and SHG beams. The relative phase was varied. (a) and (d) $\varphi(t) = 0\ rad.$ (b) and (e) $\varphi(t) = \pi/2$. (c) and (f) $\varphi(t) = \pi$.

the experimentally generated beam where the phase matching condition was manipulated to control the coefficients of the different modes.

The SHG process is performed using a PPLN crystal. The period of the grating through the crystal was $6.93\ \mu m$, and the phase matching temperature was $60.4\ ^{\circ}$C. The PPLN's dimensions are $1\ mm$ x $1\ mm$ x $20\ mm$. The beam at the output of the PPLN crystal can be considered as the superposition of three LG modes shown in (5).

III. Data Modulation and Recovery

To modulate information on the beam, the data signal is applied to an electro-optic phase modulator (NIR-MPX-LN-10) with a 12 GHz 3 dB bandwidth. The signal is applied using a Tektronix 70000B arbitrary waveform generator (AWG). This technique modulates the data on the relative phase between the two LG modes. The data signal is defined by

$$s(t) = \sum_{n=-\infty}^{\infty} a_{In}\sqrt{2}rect(t - nT_s)\cos(2\pi f_c t) + a_{Qn}\sqrt{2}rect(t - nT_s)\sin(2\pi f_c t) \tag{10}$$

where a_I and a_Q are the amplitude values for the in-phase and quadrature components of the Quadrature Amplitude Modulation (QAM) signal, respectively, $f_s = 1/T_s$ is the symbol rate of 5 GHz, and f_c is the center frequency of the signal, 7.5 GHz. To generate the signal, the RF generic signal waveform plug in on the Tektronix AWG70000B was used. A root raised cosine filter was used to perform matched filtering between the transmitter and receiver. At the receiver, a Tektronix oscilloscope using SignalVu version 3.23.0022 showed successful recovery of the measured signal. To account for the frequency response of the system, a pre-compensation was performed through the free space setup. This mitigated against the higher attenuation at specific frequencies. The signal defined by (10) is applied to the high bandwidth phase modulator which allows the signal to induce a relative phase difference between the two OAM modes in the pump beam. The signal has a uniform amplitude which is scaled to specific voltages using V_{pp}. Use of the electro-optic phase modulator allows the amplitude modulation to become phase modulation. The PM applies the signal to one branch of the interferometer. This results in the manipulation of the relative phase between the two OAM modes which are coherently combined at the output of the interferometer. As the relative phase is manipulated, the pump beam will rotate. The IG beam will rotate following the pump beam as seen in Fig. 4. The baud rates achieved for the system are 20 Gbit/s and 25 Gbit/s for 16 QAM and 32 QAM respectively. The peak-to-peak voltage, V_{pp}, of the signal directly impacts the phase delay applied to the beam. The voltage required for the modulator to apply a phase delay of π rad, V_π, is 4.4 V. When the signal is modulated into the phase, it becomes

$$\varphi(t) = \pi\frac{V_{pp}s(t)}{V_\pi} \tag{11}$$

Simulations where the relative phase between the LG modes is controlled are shown in Fig. 4. Fig. 4(a)–(c) shows the beam profiles for the fundamental wavelength while Fig. 4(d)–(f) shows beam profiles for the SHG wavelength or IG beam. The relative phase was set to three different values, 0 rad for Fig. 3(a) and (d), 0.5π rad for Fig. 4(b) and (e), and π rad for Fig. 4(c) and (f). Controlling the relative phase of the fundamental beam caused the beam to rotate to an angle of $\varphi(t)/2$.

The modulation range of the signal is determined by the total rotation of the beam. By considering the modulation range necessary to use a single detector in the recovery of the signal [18], the modulation range, h, can be determined by

$$h = \frac{V_{pp}}{2V_\pi} \tag{12}$$

Error vector magnitude (EVM) is measured as the difference between the received and theoretical constellation locations. [19]. Fig. 5. shows the effect modulation range has on EVM.

These measurements were taken through free space. The optimal modulation range for high signal-to-noise ratio (SNR) while maintaining a linear approximation at the receiver is between 0.11 and 0.14. To maintain this approximation, the modulation range of $h = 0.125$ was chosen [18]. The total rotation induced in the IG beam will be $\pm\pi h/2$ rad. From (8), the signal can be seen to cause a rotation of the IG beam. By measuring the correlation using the setup in Fig. 6(a), the power in the correlation spot is measured. The AC component of this power was controlled using the modulation range, but it remained the same for both modulation schemes. The differences in EVM for the two modulation schemes are due to power fluctuation of the fiber amplifier. A temporary reduction in the output power would reduce the optical AC power of the correlation spot leading to

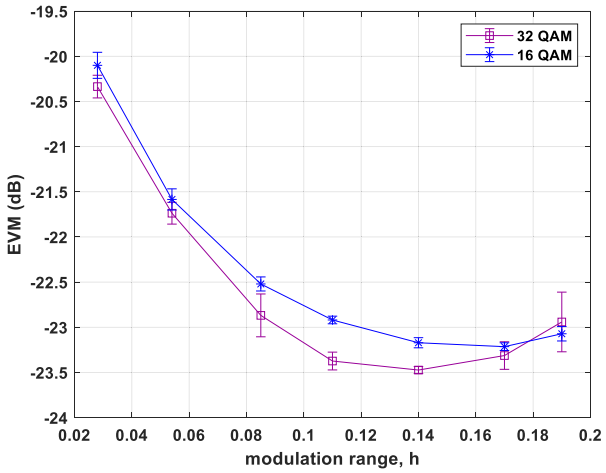

Fig. 5. The EVM of the received signal was measured as the modulation range was increased. Shown are the plots for 32 QAM and 16 QAM.

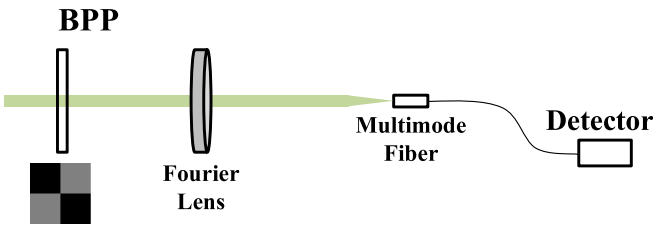

Fig. 6. The diagram of the receiver set up used to perform correlation using passive optics.

an increase in EVM. To reach the minimum EVM in the 16 QAM case, h would be larger. This minimum value would have a higher EVM due to the nonlinear region of the correlation. The minimum SNR required to recover the 32 and 16 QAM signals are 18.2 dB and 15.2 dB, respectively. The key metric in recovering a signal is a bit error ratio (BER) which is below the forward error correction (FEC) limit. The FEC limit is the probability of demodulating an incorrect bit.

To recover the signal at the receiver, a correlation using passive optics was performed. Fig. 6 shows the diagram of the receiver setup. A four-petal binary phase plate (BPP) performs a correlation with the IG beam. For different regions, the BPP will take on values of 1 or -1 as shown in Fig. 6. The correlation plate applied had a phase of 0 in two petals and a phase of π in the remaining two. Considering the decomposition of the IG beam from (5), and by knowing the rotation is only due to the LG_0^2 and LG_0^{-2} modes, this four petal BPP would correlate with these two modes while rejecting the radial mode present.

The correlation spot had a diameter of 60 μm. A multimode fiber with a 50 μm core diameter was used as a spatial filter in the Fourier plane to measure the correlation. The fluctuation of the intensity of the correlation spot will match the signal applied to the phase modulator. Using a pin with a transimpedance amplifier (TIA) for the detector, the power coupled through the fiber is recovered. As the incident beam on the BPP rotates, the correlation spot varies between a minimum and maximum seen from the simulations in Fig. 7. The white circle indicates the

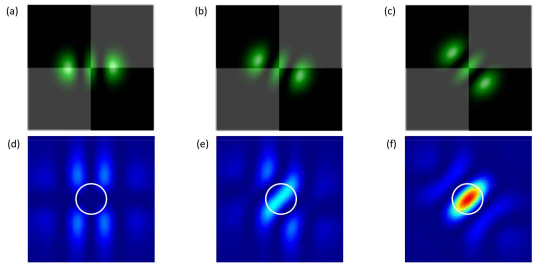

Fig. 7. Simulated beam profiles overlayed with the BPP are shown in (a)-(c). Correlation spots are shown in (d)-(f). The relative angle between the IG beam and the BPP are (a), (d) 0, (b), (e) $\pi/8$, and (c), (f) $\pi/4$. The white circle indicates the aperture generated by the multimode fiber.

aperture generated by the multimode fiber. Fig. 7(a)–(c) show the beam rotation relative to the BPP. The correlation spots generated for each orientation are shown below the beam profile in Fig. 7(d)–(f).

The on-axis correlation power determines how closely the incident mode matches the phase structure of the BPP. The correlation peak power on the detector can be estimated by [20]

$$\begin{aligned} P(t) \approx & \left| \int_{r=0}^{\infty} \left[\int_{\theta=0}^{\frac{\pi}{2}} IG_{22}^{e}(r,\theta,t)\, d\theta \right. \right. \\ & - \int_{\theta=\frac{\pi}{2}}^{\pi} IG_{22}^{e}(r,\theta,t)\, d\theta + \int_{\theta=\pi}^{\frac{3\pi}{2}} IG_{22}^{e}(r,\theta,t)\, d\theta \\ & \left. \left. - \int_{\theta=\frac{3\pi}{2}}^{2\pi} IG_{22}^{e}(r,\theta,t)\, d\theta \right] r dr \right|^2 \\ \approx & \left| 8c_{|2|} \exp(i\varphi(t)) \int_{r=0}^{\infty} A_{|2|,0} r dr \right|^2 \sin^2(\varphi(t)) \end{aligned} \tag{13}$$

The correlation of the IG beam with each region of the BPP is solved by using four integrals over the different regions of the BPP. Solving this integral shows that the power is proportional to a sinusoidal function which is dependent on $\varphi(t)$. The $\sin^2(\varphi(t))$ term which influences the correlation power can be solved using a cosine double angle formula. This cosine function can be replaced with a sine by rotating the BPP relative to the IG beam. The DC component of the optical correlation power was removed by using an AC coupled detector shown in Fig. 6. Using numerical analysis, the maximum correlation power on the detector is approximately 18% of the total power in the IG beam. Rotating the BPP to ensure a linear modulation range will reduce this power to approximately 8% of the power in the IG beam through a given attenuation length. Using (11) and (12), the optical AC power at the detector can be found in terms of the modulated signal, *s(t)*.

$$P(t) \approx 0.08 P_{in} e^{-cz} \sin(4\pi h s(t)) \tag{14}$$

where P_{in} is the input optical power of the IG beam before the channel, cz is the attenuation length, h is the modulation range, and $s(t)$ is the modulated signal with a range of ± 1. Using a Taylor Series expansion on (14) demonstrates the ability to recover the input signal with a first order approximation. This approximation allows the received power to be recovered

Fig. 8. The double pass through a 3 m underwater channel. The effects of scattering can be seen in the light illuminating the walls of the tube.

using a single receiver where previously multiple receivers were required [8], [9]. Because the beam does not need to be split for multiple detectors, the power penalty of the receiver will be much lower. This also reduces the complexity of the receiver. As only the variations of the power in the correlation spot matter, it is possible to consider the change in power, ΔP, for the different turbidity conditions. In the clear water case, the optical ΔP was 1.2 mW to prevent saturation of the detector. Through a cz of 4.5, the optical ΔP was 200 μW. To recover the signal, the high bandwidth detector generates a voltage which can be sampled using an MSO 71254C oscilloscope. There is a linear relationship between the received optical power and the recovered voltage,

$$v\left(t\right) = 0.32 P_{in} R_{532} G \pi h s\left(t\right) e^{-cz} \tag{15}$$

where $R_{532} = 0.2\ A/W$ is the responsivity of the detector to the wavelength of incident light, which in this case is 532 nm, $G = 460\ V/A$ is the gain of the internal amplifier of the detector, *h* is the modulation range and *s(t)* is the original signal containing the a_I and a_Q values of each symbol. The detector had an NEP of 47.25 $pW/\sqrt{HZ}$ at 532 nm, which provides an optical noise power of 47 μW.

Fig. 8 shows the channel used to replicate the turbid environments seen in the real world.

To replicate the underwater environment, a double pass transmission through a 3 m tube was used. To accurately replicate real-world underwater turbidity, a solution containing equate antacid can be used [21]. By increasing the amount of antacid, the turbidity level can be varied. The effects of the scattering can be seen in the illumination of the walls of the channel. One of the main benefits of performing an optical correlation is phase discrimination which occurs in the correlation plane. Therefore, any scattered light incident on the receiver will appear outside the fiber aperture.

IV. Results and Discussion

The received QAM signal is demodulated by mixing $v(t)$ with $\sqrt{2}\cos(2\pi f_c t)$ and $-\sqrt{2}\sin(2\pi f_c t)$ to recover the in phase and quadrature components which are then used to generate the constellations. The relationships between EVM, SNR, and BER

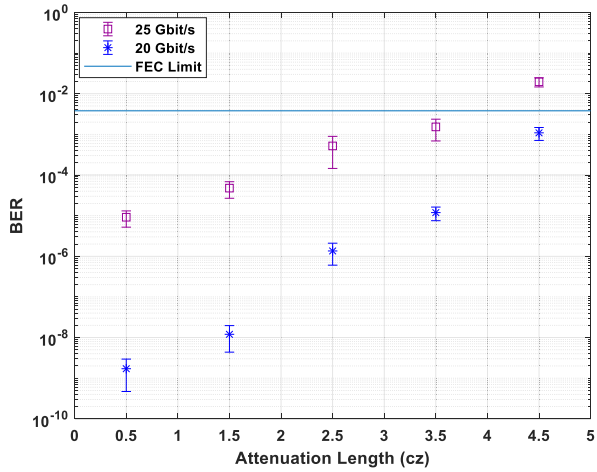

Fig. 9. The average BER for both modulation schemes, 16 and 32 QAM, as the scattering was increased. cz was varied from 0.5 to 4.5 in steps of 1. The FEC limit indicates the point where the signal is no longer recoverable.

are given by [19]

$$SNR_{rms} \approx \frac{1}{\left(EVM_{rms}\right)^2} \tag{16}$$

and

$$BER = \frac{\left(1 - M^{-\frac{1}{2}}\right)}{\frac{1}{2}\log_2\left(M\right)}\, erfc\left[\sqrt{\frac{3/2}{\left(M-1\right) EVM_{rms}^2}}\right] \tag{17}$$

where M is the number of points in the constellation, *erfc* is the complementary error function, and EVM_{rms} is the rms EVM calculated from the received I and Q components of each bit. For the 16 QAM signal, M is 16; for the 32 QAM signal M is 32. The FEC limit can be used to determine the point when a signal is no longer recoverable. Using the FEC limit of 0.0038, the minimum SNR required to recover each of the signals was calculated. For the 16 QAM signal, the minimum SNR is 15.2 dB. For the 32 QAM signal, the minimum SNR is 18.2 dB.

The experimental BERs for different cz values were collected and are displayed in Fig. 9. The cz of the channel was increased in steps of 1 starting with transmission through clear water. The total length of the underwater channel was 6 m giving a starting cz of 0.5. As the attenuation of the channel increases, the average BER can be seen to increase as well. The blue line indicates the FEC limit. The 16 QAM signal is recoverable for all cz levels measured. Because the minimum SNR required to recover the 32 QAM signal is higher than that of the 16 QAM signal, the BER of the 32 QAM signal increases above the FEC limit before that of the 16 QAM signal. At a cz of 4.5, the 32 QAM signal could no longer be recovered. The increasing attenuation length corresponds to a decrease in the power at the receiver. This supports the reduction in SNR as the attenuation length increases.

The power incident on the receiver was measured before the fiber. This power includes both the signal and noise power. Fig. 10 shows this measured power compared to the theoretical power according to Beer's Law. As cz increases, the measured power deviates from Beer's Law because of scattering. The

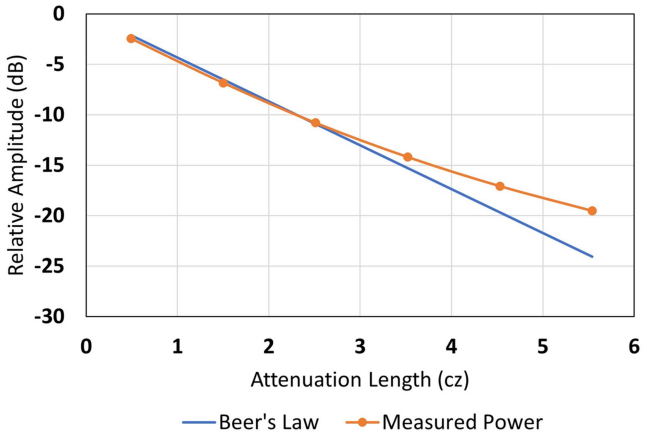

Fig. 10. The power measured at the receiver is plotted as cz increases. The received power closely matches the theoretical power according to beer's law.

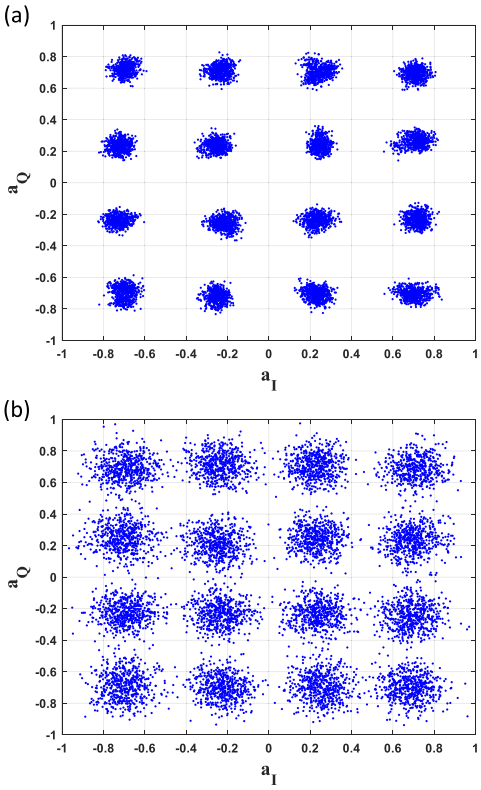

Fig. 11. Constellations of the 16 QAM signal through (a) clear water with a BER of 2.99×10^{-10} and (b) a cz of 4.5 with a BER of 1.1×10^{-3}.

turbidity in the underwater channel increases the scattered light into the measuring aperture. While the power incident on the receiver is higher, the scattered light will not correlate through the filter.

The constellations shown in Figs. 11 and 12 provide visual illustrations for the quality of the data received. The SNR of the signal propagating through clear water was 22.8 dB for both modulation schemes. The optical power through clear water was decreased to prevent saturation of the detector. By encoding the information in the rotation of the IG beam, scattered photons

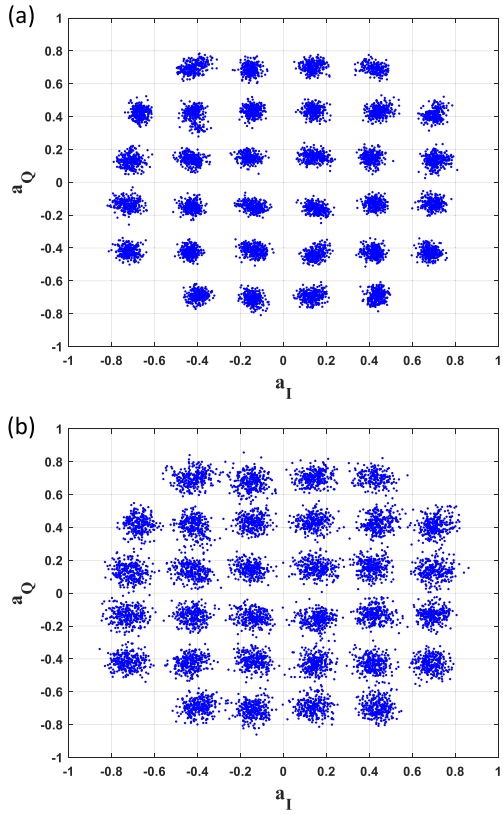

Fig. 12. Constellations of the 16 QAM signal through (a) clear water with a BER of 6.13×10^{-6} and (b) a cz of 3.5 with a BER of 7.96×10^{-4}.

will not correlate at the receiver. The reduction in SNR is due to a reduction of ballistic photons collected by the correlator rather than an increase in noise due to temporal scattering. The SNR at a *cz* of 3.5 where both signals were recoverable was 19.8 dB. At a *cz* of 4.5, the SNR decreased further to 16.4 dB. Maintaining the same SNR for both signals results in a higher BER for the 32 QAM signal.

The constellations in Fig. 11 compare the 16 QAM signal through clear water, Fig. 11(a), to the signal through a *cz* of 4.5, Fig. 11(b). The BER increased from 2.99×10^{-10} to 1.1×10^{-3} with the increased scattering. The constellations in Fig. 12 compare the 32 QAM signal through clear water, Fig. 12(a), to the signal through a *cz* of 3.5, Fig. 12(b). The BER increased from 6.13×10^{-6} to 7.96×10^{-4} with the increase in the scattering media. The increase in BER is observable in the spreading of the constellation points. As the constellation spots begin to spread and overlap with other spots reducing the certainty of the received bit combination.

By utilizing the IG_{22}^{e} beam as the carrier for data transmission using constant envelope modulation techniques, it would be possible to scale this system through the use of multiple channels. One method which could demonstrate this would utilize polarization techniques where one channel would have horizontal polarization while another would have vertical polarization. These two channels could be easily separated at the receiver. Another method to increase the number of channels would be through the coherent combination of multiple IG_{22}^{e} beams. Due

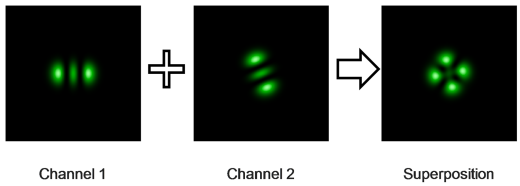

Fig. 13. The scalar superposition of two IG beams. The superposition can be considered a coherent combination of IG beams.

to the propagation invariance and the small rotation of the beam during modulation, two beams with different orientations could be coherently combined to transmit multiple channels. Fig. 13 shows the resulting beam profile of the coherently combined IG beams. The data of each channel could be recovered using similar correlation techniques.

V. Conclusion

This article demonstrated the use of a nonlinear process to generate IG beams which were used as the carrier beam for underwater free space communication through turbid environments. The SHG process was performed with a PPLN crystal which had a controllable phase matching condition based on temperature, allowed for a power scalable system, and generated a high power 532 nm beam which mitigated absorption in underwater environments. Controlling the phase matching condition allows the coefficients of the output modes to be manipulated. Modulation of the data on the relative phase between the pump modes results in a rotation of both the pump beam and the IG beam. Using this modulation technique, a 25 Gbit/s communication link through a turbid, underwater channel which replicates coastal ocean environments was performed. As discussed, the system demonstrated has significant scalability due to polarization and superposition techniques. Multiple channels with high bandwidth signals could be transmitted simultaneously. The constant envelope modulation technique allows the power of the system to be increased without introducing issues of high PAPR The robustness of IG beams when propagating through turbid environments allows them to perform well as a carrier for communication systems. These benefits may also exist when studying propagation through atmospheric turbulence or the air water interface. Using this technique, the complexity of the receiver is reduced by using a single detector. This also prevents the power penalty from optical detection schemes using 2 or more detectors. It is unclear about the impact of scattering on this modulation scheme compared to direct modulation techniques; however, the narrow field of view provided by the correlator separates the ballistic and scattered photons for enhanced discrimination. We believe this modulation method may offer benefits when propagating the beam through scattering media.

References

[1] S. Zhu, X. Chen, X. Liu, G. Zhang, and P. Tian, "Recent progress in and perspectives of underwater wireless optical communication," *Prog. Quantum Electron.*, vol. 73, 2020, Art. no. 100274, doi: 10.1016/j.pquantelec.2020.100274.

[2] S. Al-Zhrani et al., "Underwater optical communications: A brief overview and recent developments," *Engineered Sci.*, vol. 16, pp. 146–186, 2021.

[3] Y. Ata and O. Korotkova, "Absorption, scattering, and optical turbulence in natural waters," *Appl. Opt.*, vol. 61, pp. 4404–4411, 2022.

[4] K. Dai et al., "Impulse response of OAM beams propagating through turbid underwater environments," in *Proc. Imag. Appl. Opt. Congr.*, 2022, Paper. PTh3F.2.

[5] J. Baghdady et al., "Multi-gigabit/s underwater optical communication link using orbital angular momentum multiplexing," *Opt. Exp.*, vol. 24, pp. 9794–9805, 2016.

[6] Y. Ren et al., "Orbital angular momentum-based space division multiplexing for high-capacity underwater optical communications," *Sci. Rep.*, vol. 6, 2016, Art. no. 33306.

[7] K. Morgan, K. Dai, J. K. Miller, C. O'Donnel, R. J. Watkins, and E. G. Johnson, "Free-space underwater constant-envelope orthogonal frequency division multiplexing using phase modulation of orbital angular momentum modes," in *Proc. IEEE Int. Conf. Commun. Workshops*, 2020, pp. 1–6.

[8] K. Morgan, Y. Li, W. Li, J. K. Miller, R. J. Watkins, and E. G. Johnson, "Multilevel quadrature amplitude multiplexing using coherently coupled orbital angular momentum modes," *Opt. Exp.*, vol. 26, pp. 12180–12190, 2018.

[9] Y. Li, K. Morgan, W. Li, J. K. Miller, R. Watkins, and E. G. Johnson, "Multi-dimensional QAM equivalent constellation using coherently coupled orbital angular momentum (OAM) modes in optical communication," *Opt. Exp.*, vol. 26, pp. 30969–30977, 2018.

[10] J. K. Miller et al., "Underwater optical communication link using polarization division multiplexing and orbital angular momentum multiplexing," in *Proc. OCEANS Anchorage*, 2017, pp. 1–4.

[11] Z. Li et al., "Robust transmission of Ince-Gaussian vector beams through scattering medium," *Optik*, vol. 257, 2022, Art. no. 168766.

[12] E. N. Casañeda, J. Vázquez, R. Alarcón, I. Agha, Q. Zhan, and W. N. Plick, "Ince-Gauss beams in a turbulent atmosphere: The effect of structural parameters on beam resilience," *Opt. Continuum*, vol. 1, pp. 1777–1794, 2022.

[13] M. A. Bandres and J. C. Gutiérrez-Vega, "Ince-Gaussian beams," *Opt. Lett.*, vol. 29, pp. 144–146, 2004.

[14] G. Walker, A. S. Arnold, and S. Franke-Arnold, "Trans-spectral orbital angular momentum transfer via four-wave mixing in Rb vapor," *Phys. Rev. Lett.*, vol. 108, 2012, Art. no. 243601.

[15] R. N. Lanning, Z. Xiao, M. Zhang, I. Novikova, E. E. Mikhailov, and J. P. Dowling, "Gaussian-beam-propagation theory for nonlinear optics involving an analytical treatment of orbital-angular-momentum transfer," *Phys. Rev. A*, vol. 96, 2017, Art. no. 013830.

[16] J. C. A. Rocha, D. G. Pires, J. G. M. N. Neto, A. J. Jesus-Silva, N. M. Litchinitser, and E. J. S. Fonseca, "Speckle filtering through nonlinear wave mixing," *Opt. Lett.*, vol. 46, pp. 3905–3908, 2021.

[17] R. F. Offer, A. Daffurn, E. Riis, P. F. Griffin, A. S. Arnold, and S. Franke-Arnold, "Gouy phase-matched angular and radial mode conversion in four-wave mixing," *Phys. Rev. A*, vol. 103, 2021, Art. no. L021502.

[18] A. U. Ahmed and J. R. Zeidler, "Novel low-complexity receivers for constant envelope OFDM," *IEEE Trans. Signal Process.*, vol. 63, no. 17, pp. 4572–4582, Sep. 2015.

[19] R. A. Shafik, M. S. Rahman, and A. R. Islam, "On the extended relationships among EVM, BER, and SNR as performance metrics," in *Proc. Int. Conf. Elect. Comput. Eng.*, 2006, pp. 408–411.

[20] K. Dai, J. K. Miller, J. Free, M. Lemon, F. Dalgeish, and E. G. Johnson, "Remote sensing using a spatially and temporally controlled asymmetric perfect vortex basis generated with a 2D HOBBIT," *Opt. Exp.*, vol. 30, no. 19, pp. 34765–34775, 2022.

[21] F. Hanson and S. Radic, "High bandwidth underwater optical communication," *Appl. Opt.*, vol. 47, pp. 277–283, 2008.